

Optical Engineering

SPIDigitalLibrary.org/oe

Nondestructive testing potential evaluation of a terahertz frequency- modulated continuous-wave imager for composite materials inspection

Edison Cristofani
Fabian Friederich
Sabine Wohnsiedler
Carsten Matheis
Joachim Jonuscheit
Marijke Vandewal
René Beigang

Nondestructive testing potential evaluation of a terahertz frequency-modulated continuous-wave imager for composite materials inspection

Edison Cristofani,^{a,*} Fabian Friederich,^b Sabine Wohnsiedler,^b Carsten Matheis,^b Joachim Jonuscheit,^b Marijke Vandewal,^a and René Beigang^b

^aRoyal Military Academy, CISS Department, Av. de la Renaissance 30, B-1000 Brussels, Belgium

^bFraunhofer-IPM, Institute for Physical Measurements Techniques, Erwin-Schroedinger Street 56, D-67663 Kaiserslautern, Germany

Abstract. The sub-terahertz (THz) frequency band has proved to be a noteworthy option for nondestructive testing (NDT) of nonmetal aeronautics materials. Composite structures or laminates can be inspected for foreign objects (water or debris), delaminations, debonds, etc., using sub-THz sensors during the manufacturing process or maintenance. Given the harmless radiation to the human body of this frequency band, no special security measures are needed for operation. Moreover, the frequency-modulated continuous-wave sensor used in this study offers a very light, compact, inexpensive, and high-performing solution. An automated two-dimensional scanner carrying three sensors partially covering the 70- to 320-GHz band is operated, using two complementary measurement approaches: conventional focused imaging, where focusing lenses are used; and synthetic aperture (SA) or unfocused wide-beam imaging, for which lenses are no longer needed. Conventional focused imagery offers finer spatial resolutions but imagery is depth-limited due to the beam waist effect, whereas SA measurements allow imaging of thicker samples with depth-independent but coarser spatial resolutions. The present work is a compendium of a much larger study and describes the key technical aspects of the proposed imaging techniques and reports on results obtained from human-made samples (A-sandwich, C-sandwich, solid laminates) which include diverse defects and damages typically encountered in aeronautics multilayered structures. We conclude with a grading of the achieved results in comparison with measurements performed by other NDT techniques on the same samples. © 2014 Society of Photo-Optical Instrumentation Engineers (SPIE) [DOI: 10.1117/1.OE.53.3.031211]

Keywords: nondestructive testing; terahertz; frequency-modulated continuous-wave; synthetic aperture; laminate; glass-fiber; glass fiber reinforced plastics; carbon fiber reinforced plastics; composite.

Paper 131000SSP received Jul. 2, 2013; revised manuscript received Feb. 19, 2014; accepted for publication Feb. 28, 2014; published online Mar. 21, 2014.

1 Introduction

In recent years, the development of terahertz (THz) systems has made considerable progress and made possible a variety of innovative applications.¹ Among them, nondestructive testing (NDT) of composite materials can take advantage of the high transparency of certain nonconductive materials²⁻⁶ at sub-THz frequencies. The presence of such materials is foreseen to increase in the next years, especially in aeronautics. Glass-fiber (GF) laminates or composite structures are currently being used due to their outstanding structural properties, durability, and lightness. In response to the growing industrial interest in these materials, a THz inspection system was developed and exploited on human-made calibration and blind samples, which replicated the most commonly encountered defects in aeronautics laminates and composites for performance evaluation purposes. The system is based on a two-dimensional (2-D) automatic scanner carrying three wideband frequency-modulated continuous-wave (FMCW) sub-THz transceivers, operating at the center frequencies of 100, 150, and 300 GHz. This configuration allows three-dimensional (3-D) in-depth imaging of flat samples and, hence, in-depth defect inspection.

Although pulsed broadband THz imaging systems based on time-domain spectroscopy setups could provide better lateral and axial resolutions, the depth information is given by the time-of-flight of the THz pulse, which is measured by the use of a variable delay line to sample the THz pulse in the time domain. The required length of the delay line depends on the thickness of the sample and thereby restricts the pixel acquisition rate, which can be on the order of 20 Hz for samples of several millimeters to centimeters thickness in combination with a fast delay mechanism.⁷ Since the investigations within the underlying study have shown a strongly decreasing THz transmittance of the present materials under test at frequencies of above 300 GHz, the reachability of better image resolutions is limited. In contrast, the used FMCW sensors are less complex, highly compact, inexpensive, and provide high sensitivities even at measuring rates of 4 kHz. Two complementary imagery approaches based on the FMCW system are presented in this work: conventional or focused configuration and synthetic aperture (SA) or unfocused configuration.

On the one hand, the focused configuration is based on a set of lenses, which are used to focus the emitted THz beam onto or into the test sample; as well as the transmitted radiation back to the sensors for signal detection. Due to the

*Address all correspondence to: Edison Cristofani, E-mail: edison.cristofani@elec.rma.ac.be

focusing of the beam, the spatial resolution varies with the inspected range. Consequently, a high image resolution with strong signal amplitudes can be acquired within the focal plane, whereas for thicker samples only partial in-depth information can be obtained in one single scan.

On the other hand, focusing lenses are not necessary in the SA configuration. Instead, appropriate digital signal processing must be applied in order to focus the received wide-beam signals in software. SA imagery offers a constant spatial resolution regardless of the depth imaged although, by definition, resolution is significantly coarser than in focused configurations. This approach allows inspecting thicker samples and a simpler calibration, and has been successfully tested by the authors⁸⁻¹¹ as well as by other research groups.¹²

The main objective of this study is to present the potential of state-of-the-art, THz-FMCW imagery as an affordable and high-performing NDT method, taking into account both the conventional and innovative approaches (focused and SA configurations, respectively). This work will present results from a comprehensive collection of composite materials and implemented defects and, therefore, will provide a general overview of the current capabilities of this method on composites which, to the authors' knowledge, have been described separately in the literature.¹³⁻¹⁸

Given these two approaches, their intrinsic complementary properties can be combined to satisfactorily cover most of the composite material inspection situations. Representative results will be described for both approaches, and conclusions from comparisons to measurements performed by THz-TDS systems and other conventional inspection techniques on the same samples will be drawn. This work is divided as follows: Sec. 2 provides a description of the focused imaging approach as well as technical details of the used sub-THz sources. Section 3 describes the SA wide-beam configuration as well as the required signal processing. Section 4 presents results using the two proposed THz-NDT techniques on a collection of representative aeronautics composites. Section 5 will finally detail all conclusions reached.

2 Conventional Focused NDT System

2.1 Focused Setup Description

The present THz-FMCW system can be operated in reflection as well in transmission mode with up to three different frequency ranges simultaneously. Therefore, the system houses up to six sensor heads (Fig. 1), whereas three of them are receiver units which face three transceiver heads for transmission measurements. Each sensor head has external dimensions of $230 \times 75 \times 75$ mm.

Although the test sample is fixed in the center of the setup between the transceiver and receiver modules, the sensor heads perform a vertical 2-D raster scan within a scan area of up to 600×600 mm. The minimum step size is 0.5 mm both horizontally and vertically, whereas a measuring rate of up to 4 kHz in the azimuth direction can be achieved. Within this study, the typical overall measurement time for a 200×300 -mm sample was below 30 min using 1-mm steps in elevation and an acquisition speed of 0.5 m/s in the azimuth direction. Before each measurement, a sensor calibration is performed, which ensures proper

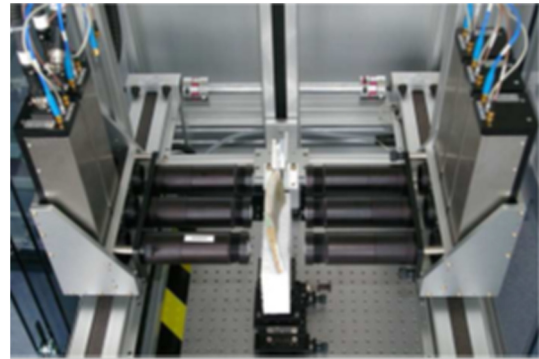


Fig. 1 Picture of the complete frequency-modulated continuous-wave (FMCW) radar system and a sample material being imaged. A total of six modules are used for reflection and transmission modes.

operation of the sensor and allows setting the z -scale and the scale of the signal amplitude for the image appearance. For this purpose, a set of vertical planes in a fixed distance serve as perfect back-reflectors, and another reflector is used to divert the transmitted beam for zero-reflection calibration.

2.2 FMCW Signal Generation

The transceiver heads are used for measurements in transmission and reflection mode, whereas exclusively the latter were performed within the present work. Each of the transceivers comprises a voltage-controlled oscillator (VCO) which drives a micro-electronic multiplier chain for THz generation and a single diode-based harmonic mixing module. Within the mixer, the VCO signal is multiplied and superimposed with the received THz signal for heterodyne detection. As depicted in Fig. 2, the THz radiation is sent and received through a single horn antenna by using a directional coupler, which is connected to the source and the detector unit. Additionally, the signal of the VCO can be fed to the corresponding receiver head for transmission mode

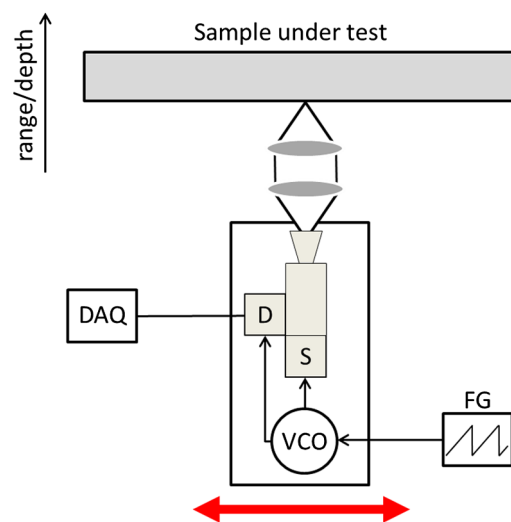


Fig. 2 Schematic of the FMCW setup in focused configuration; a function generator is used to linearly ramp a voltage-controlled oscillator which drives the transceiver [source (S) and detector (S), respectively]. The mixer output of the detector is recorded by a data acquisition unit, which is synchronized with the x , y -translation stages.

measurements, which have not been used in the underlying study.

The signal frequency of the VCO is modulated in a range between 13 and 18 GHz by a saw-tooth ramp generator and is up-converted by the frequency multiplier chain to the operation frequency range, as detailed in Table 1. The system has been configured to achieve a single 250-μs frequency sweep.

In the conventional focused configuration, a set of quasi-optical Teflon lenses is used to focus the emitted THz radiation into the test sample and the transmitted and/or reflected parts of the THz beam into the transceiver. For the given setup, the minimum spatial resolution for each sensor pair is listed in Table 1. The FMCW technique can be described by a saw-tooth-like frequency modulation as shown in Fig. 3.

The linear frequency sweep of the emitted THz radiation allows the acquisition of the time delay τ_R between the transmitted (TX) and received (RX) signal by superposition. This results in a beat signal with a frequency f_b equal to the difference frequency of the superimposed signals, which is proportional to the optical path difference in a medium with refractive index n . In respect to the period T_p and the bandwidth Δf of the frequency modulation, the distance or depth of the inspected region is described by

$$d = \frac{c}{2n} \tau_R = \frac{c f_b}{2n \Delta f}. \tag{1}$$

The achievable depth resolution is given by the bandwidth of the frequency modulation.¹⁹ The use of the FMCW technique on THz-transparent materials therefore allows the reconstruction of tomographic THz images.²⁰ In the present case, the signal path differences between the received THz radiation and the reference signal from the VCO generate beat signals with constant frequencies at the receiver output, while the above-mentioned calibration procedure ensures the required quasilinear frequency sweep of the VCO. The received mix of beat signals from different depths can be separated by Fourier analysis. The resulting spectrum reveals the amplitude of signals retrieved from different depths. For the conventional focused system configuration, it has to be taken into account that the achievable image resolution is varying with the inspected depth as the beam radius increases with the distance to the beam waist. Hence, the stronger optical signal and better lateral resolution preserved with a tighter

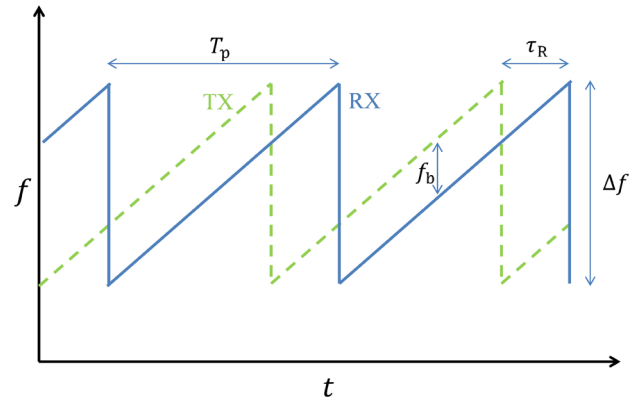


Fig. 3 Frequency evolution of the transmitted linear FMCW (solid) and received signal (dashed) from one scatterer after a time delay of τ_R seconds.

focus, opposes a smaller depth of focus, respectively, Rayleigh length and therefore a reduced range in which high-resolution images can be acquired. Within the present study, two different sets of optics for the focused imaging configuration have been used. Although Teflon lenses with 100-mm focal length were used in front of the horn antennas, lenses with 50-mm and alternatively 100-mm focal length have been used to focus into the samples.

3 SA NDT System

3.1 Wide-Beam Setup Description

The focused configuration presented in Sec. 2 can be easily adapted to an SA configuration for wide-beam measurements. Removing the focusing lenses produces beams with opening angles of ca. $\theta_{-3\text{ dB}} = 16^\circ$. The sample is placed at a distance $R_0 = 200$ mm away from the sensor to allow collecting data with sufficient power levels for further signal processing and to avoid the undesired near-field effects. Two sensors, 100 and 150 GHz, are used for SA imagery. The limited transmitted power provided by the 300-GHz sensor combined with the lower transparency of aeronautics materials in this band lead to low signal-to-noise ratios.

Figure 4 depicts how the platform is mechanically translated by the scanner following a linear measurement path in the across direction. This even sampling scheme in azimuth can be arbitrarily extrapolated to a second measurement axis,

Table 1 Specifications of the THz-FMCW system (Ref. 18).

Sensor	100 GHz	150 GHz	300 GHz
Frequency range	0.07 to 0.11 THz	0.11 to 0.17 THz	0.23 to 0.32 THz
Dynamic range (acquisition time per pixel: 100 ms)	>70 dB	>70 dB	>60 dB
Opening angle (−3 dB)	16 deg	16 deg	16 deg
Spatial resolution (focused)	3 mm	2 mm	1 mm
Spatial resolution (wide-beam)	6 mm	4 mm	N/A
Depth resolution in air	9 mm	6 mm	3 mm

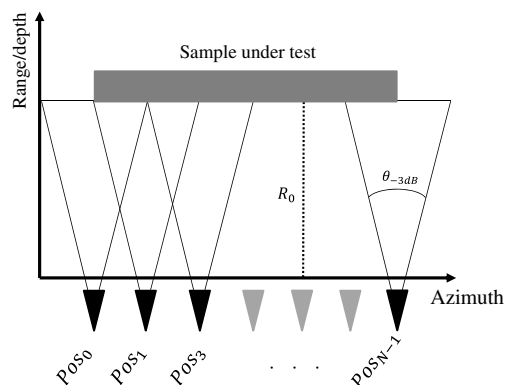


Fig. 4 Schematic representation of a measurement using a wide-beam approach. The sensor moves along a scanning path in azimuth.

i.e., elevation, in order to produce a 2-D movement that enables generating 3-D SA images of flat samples. Conventional SA processing algorithms can be adapted to reconstruct 3-D scenes.

3.2 SA Principles and Image Formation

By adequately combining wide-beam measurements equispaced in the across-range direction [Fig. 5(a)], the coarse, diffraction-limited spatial resolution of a real aperture can be improved.²¹ As a result, an antenna with a much larger aperture is synthesized, obtaining spatial resolutions that would require an equivalent real aperture antenna of an impractical physical size. SA algorithms can produce images with spatial and range resolutions as described by Eqs. (2) and (3), respectively,

$$\delta_{\text{spat}} \cong \frac{c}{2f_c \sin(\theta_{-3 \text{ dB}})} \quad (2)$$

$$\delta_r \cong \frac{c}{2\Delta f}, \quad (3)$$

where f_c and Δf are the center frequency and bandwidth of the sensor, respectively, and c is the speed of light. If compared to conventional focused systems, wide-beam systems present equal range resolutions²¹ whereas spatial resolution remains constant for all ranges, despite being significantly coarser. Therefore, the beam waist effect mentioned in Sec. 2 is avoided for materials thicker than the Rayleigh length, at the cost of less accurate images. By using SA, the maximum inspection depth is ideally limited by the available power and the sensor's sensitivity.

SA algorithms such as range-Doppler, omega-k, or time-domain back-projection^{8-11,21} algorithms integrate in a coherent way the energy spread in the across-range direction due to the hyperbolic sensor-to-scene distance function or $R(t)$. This function is the Euclidean distance between two points in a 2-D or 3-D scene. Figure 5(b) describes the theoretical response of an infinitesimal point target after range compression. The compacted energy after range compression (using matched filtering or, for FMCW systems, a Fourier transform in range¹¹) follows the hyperbolic law announced by

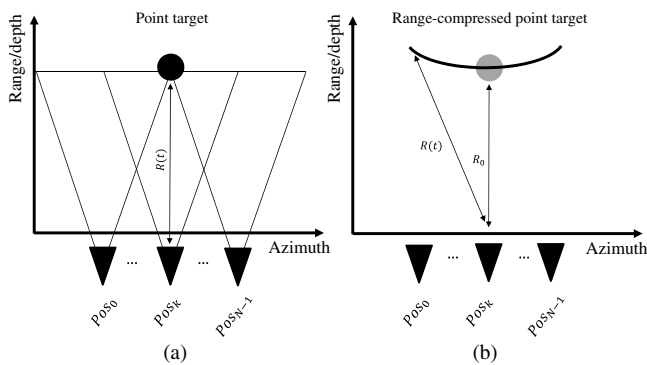


Fig. 5 (a) Theoretical point target being illuminated by a wide-beam scanning system along the cross-range direction and (b) theoretical range-compressed representation of the point target's backscattered energy.

$$R(t) = \sqrt{R_0^2 + y(t)^2}, \quad (4)$$

where $y(t) = v \cdot t$ is the sensor's position in the cross-range axis at a given slow time t and platform speed v . The hyperbolic deformation described by Eq. (4) must be compensated for in order to produce the focused SA imagery.

4 Proposed THz-NDT Techniques Results

4.1 Practical Experimental Details

During this study, flat samples including human-made defects such as inserts, stucks, water inclusions, impacts, etc. were produced and measured in order to create well-controlled and well-known samples for THz systems and algorithms validation. During the calibration stage, 20 glass fiber reinforced plastics (GFRP) samples (solid laminates and sandwich structures), and five carbon fiber reinforced plastics (CFRP) were used. In a next stage, the evaluation as a THz-NDT method has been performed on 50 blind samples (12 GFRP and 38 CFRP samples) with embedded defects caused by intentional misprocesses. Conclusions drawn in Sec. 5 are based on the obtained results.

4.2 Selected Samples Description

Representative samples in terms of structure, materials, and implemented defects were selected for measurement and discussion on the possibilities offered by THz-FMCW imagery: A-sandwiches including debonds, water inclusions on honeycomb- and Rohacell-cored C-sandwiches; and mechanic impacts inflicted to GF solid laminates. A short description of the samples used in the following sections is provided in Table 2.

4.3 Focused Imagery

Although the determination of small object features is often limited by the angular resolution, the object penetration depth of the THz radiation is typically better at larger wavelengths. However, better depth resolutions lead to a better signal contrast in the inspected volume and can therefore reveal previously unrecognized defects, as illustrated by THz measurements of sample GF_AR in Fig. 6.

Contrary to the images acquired by the 150- and 300-GHz sensor head, only a frame-like feature surrounding the real debond can be revealed by the 100-GHz module. This edge effect is also visible in the photograph of the sample and is caused by the process which is used to artificially create the defect. Although the better depth as well as spatial resolution provided by the 150- and 300-GHz sensors allow higher-signal contrast within the inspected region, revealing the debonds within the sample, the increasing absorption of the material toward higher sub-THz frequencies makes the smallest defect hardly visible.

A remarkable feature of the THz-FMCW system is the capability to inspect front-layer defects of sandwich structures from the back side and, therefore, through the core of the sample GF_AHI, as shown in Fig. 7.

The test sample GF_AHI contains different types of inserts (stucks, paper, and Teflon) which are placed in different layers of the structure. Despite that all inserts are visible in the THz image of the front side, they can also be identified in almost all back side images. Water inclusions were also

Table 2 Principal parameters defining selected samples in this study.

Sample	Structure	Core ^a	Size ($W \times H \times D$)	Defects found
GF_AR	A-sandwich	Rohacell	260 × 150 × 6 mm	Debond between skin and adhesive
GF_AHD	A-sandwich	Honeycomb	215 × 120 × 10 mm	Debond between adhesive and core
GF_AHI	A-sandwich	Honeycomb	200 × 340 × 7 mm	Inserts: various materials, sizes and depths
GF_AH035	A-sandwich	Honeycomb	150 × 75 × 7 mm	0.35-ml water inclusion
GF_CH075	C-sandwich	Honeycomb	150 × 75 × 7 mm	0.75-ml water inclusion
GF_CR075	C-sandwich	Rohacell	150 × 75 × 7 mm	0.75-ml water inclusion
GF_SL30J	GF laminate	N/A	45 × 45 × 5 mm	30-J impact
GF_SL40J	GF laminate	N/A	45 × 45 × 5 mm	40-J impact

^aCores are 5-mm thick.

detected within honeycomb sandwich structures, whereas such defects could not be inspected within comparable samples based on Rohacell cores (Fig. 8).

It can be concluded that honeycomb sandwich structures tolerate the creation of larger reflecting water boundary layers when compared to the denser Rohacell sandwiches. Regarding GF reinforced solid laminate samples, similar results can be obtained by inspecting inserts as within the aforementioned described test panel with the sandwich structure. Several delaminations were detected, although in most of the images only edge effects comparable to the ones in

Fig. 6 were measured. In addition to the determination of inserts and delaminations, impact damage inspections have been performed on these solid laminate samples, as shown in Fig. 9.

Thereby, samples that were exposed to impact energies from 15 to 40 J have been investigated. Except for the smallest impact with energy of 15 J, all impact damages could be detected.

Carbon fiber-reinforced solid laminates behave quite differently. While the inherent surface structure could only be resolved using the 300-GHz sensor head, impact damages on

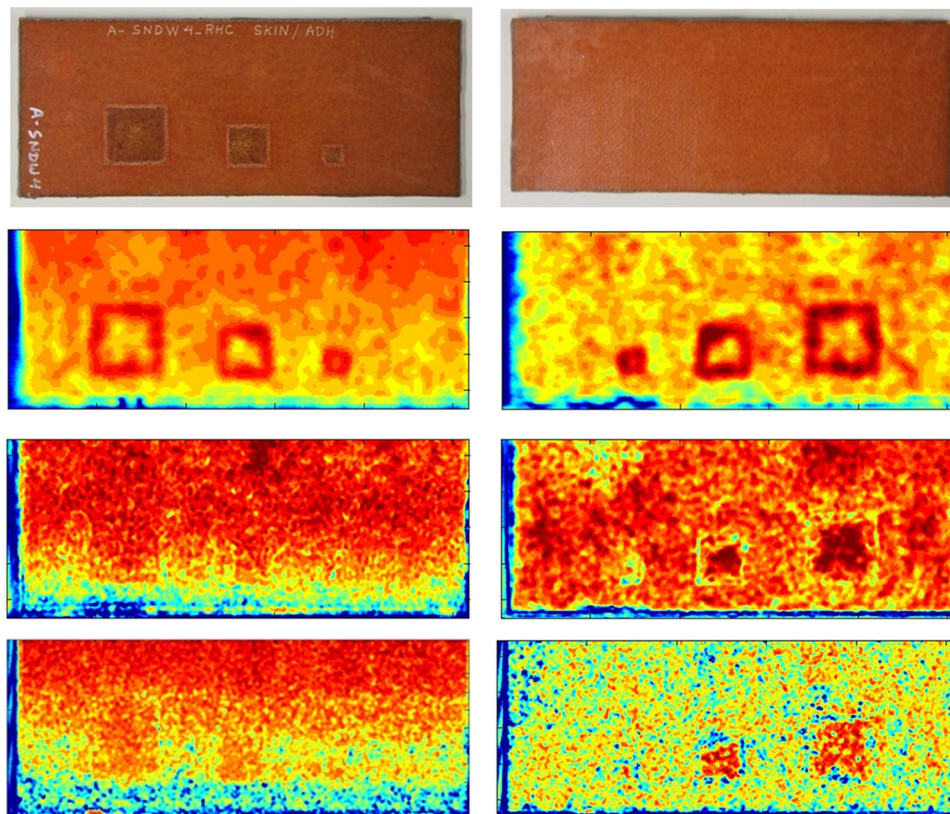


Fig. 6 Sample GF_AR, from top to bottom: photograph of the structure and THz images of the front side (left), respectively, back side (right) at 100, 150, and 300 GHz.

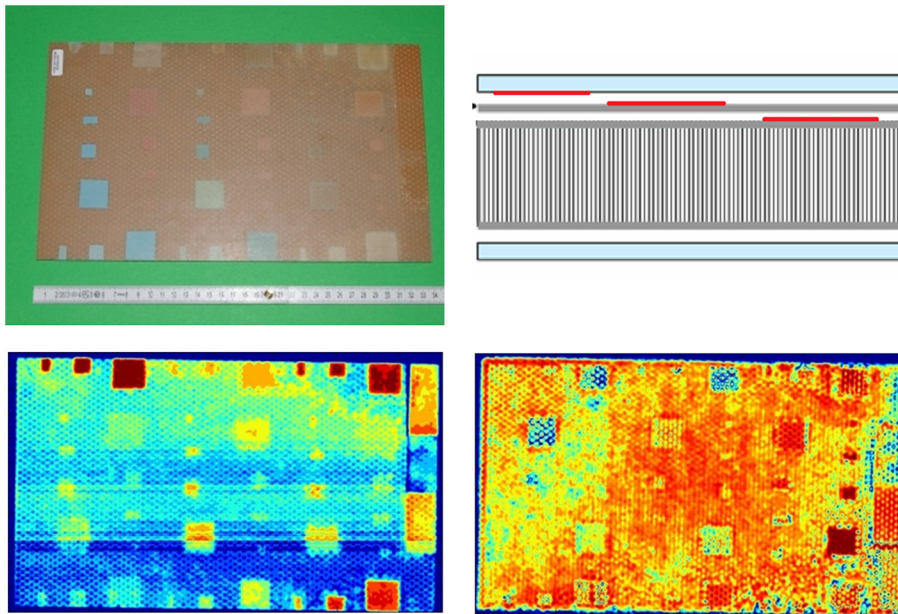


Fig. 7 Top: photograph of sample GF_AHI (left) and a scheme showing exemplary locations of the inserts in different layers (right). Bottom: THz images at 150-GHz center frequency from the front side (left) and back side (right) of the sample.

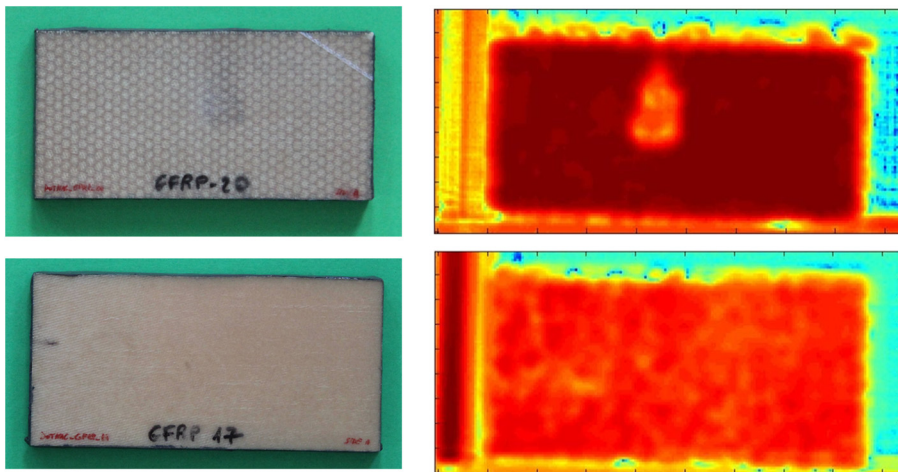


Fig. 8 Water inclusion in samples GF_CH075 (top) and GF_CR075 (bottom). The THz images to the right side were recorded at 100 GHz at the center frequency from the back side of the samples. In contrast to the upper photograph, the water inclusion is not directly visible from the back side.

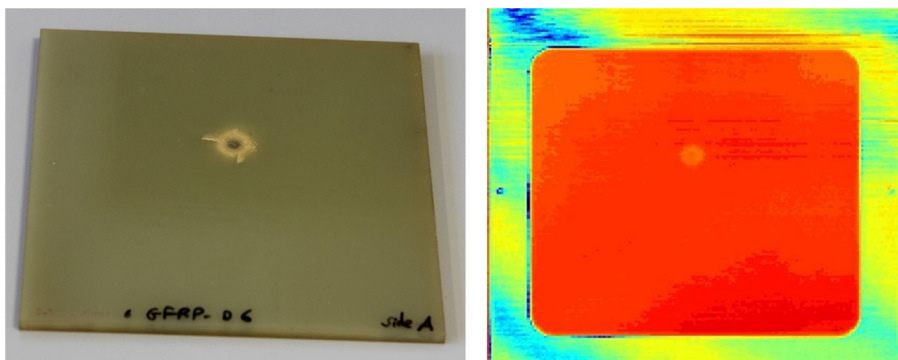


Fig. 9 Sample GF_SL40J: left, a picture; right, THz image of the impact at 300-GHz center frequency with the sample placed in a holder.

these samples could not be detected. Moreover, coating mis-processes cannot be identified by the present system.

4.4 SA Imagery

A series of composite and solid laminate samples were measured using the wide-beam approach. Representative samples are discussed next. Figure 10(a) presents a photograph of sample GF_AHD. Human-made debonds of different sizes (50×50 , 25×25 , and 12×12 mm) can be found between the adhesive layer and the core.

Images depicted in Figs. 10(b) and 10(c) show 100-GHz results using SA at depths near the front-layer and slightly deeper into the sample, respectively. The largest debonds are clearly observed showing a persistent behavior in depth, while the smallest debond is only seen at a given range, deeper in the material. The detection of these small defects is limited by the spatial resolution of the wide-beam approach, the lower backscattered energy, and the distorting effect of the honeycomb core. Likewise, in the surface plot Fig. 10(d), the smallest defect is still visible but the more accurate reconstruction of the honeycomb structure makes

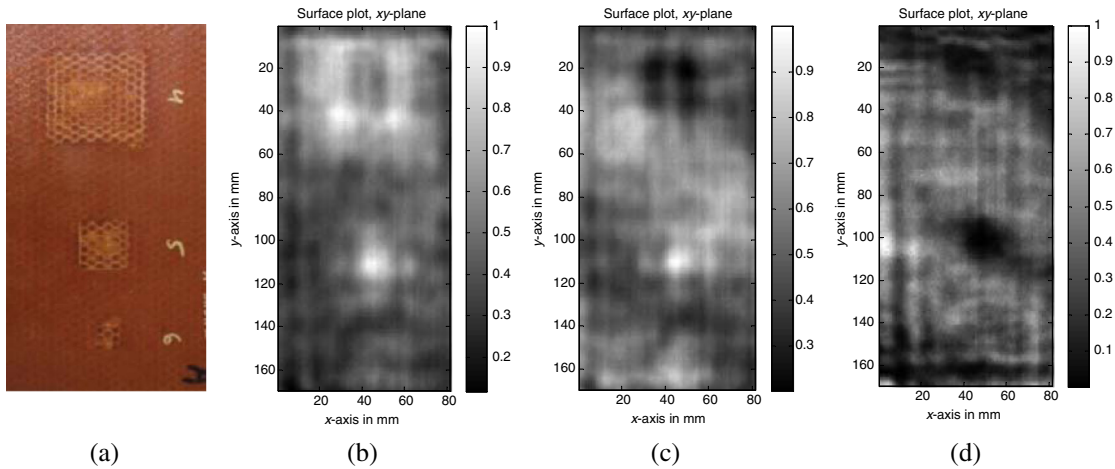


Fig. 10 Sample GF_AHD: (a) photograph of the sample. SA images of the sample: (b) surface plot of the front-layers (100 GHz); (c) surface plot at a deeper position (100 GHz); and (d) surface plot of the front-layers (150 GHz).

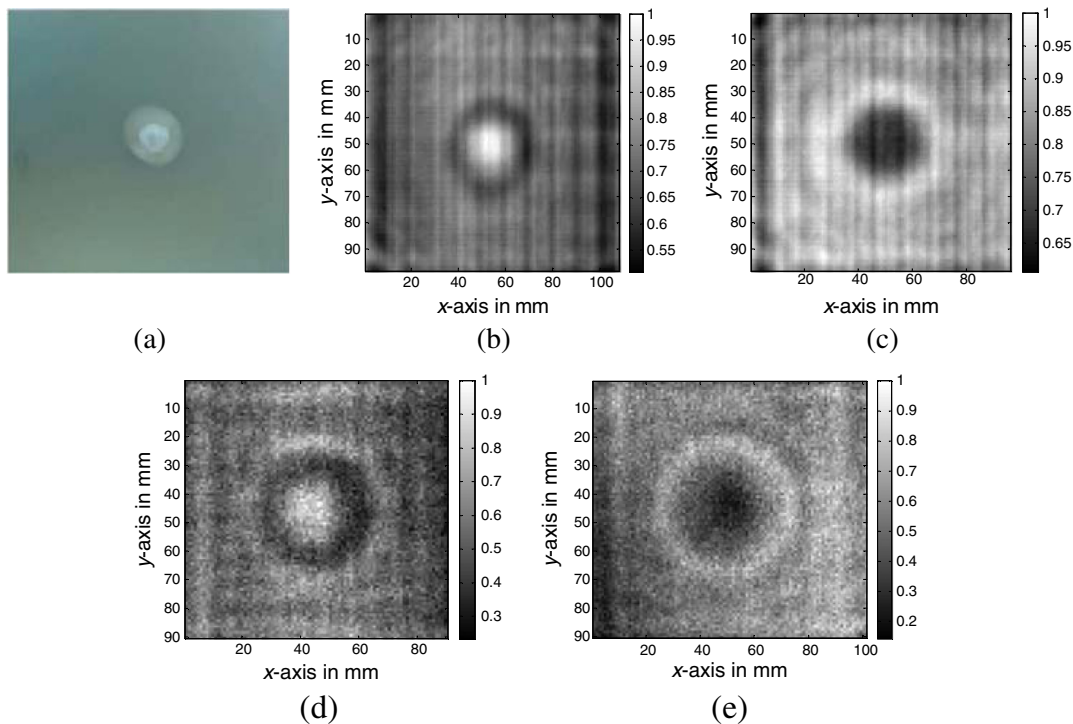


Fig. 11 Sample GF_SL30J: (a) photograph of the sample. SA images of the sample: (b) surface plot of the front side (100 GHz); (c) surface plot of the back side (100 GHz); and (d) surface plot of the front side (150 GHz); surface plot of the back side (150 GHz).

defect detection more complicated, even for a trained operator.

Figure 11(a) presents a photograph of sample GF_SL30J, a GF solid laminate which was inflicted with a 30-J impact. Several plies were affected, creating a crater-like defect in the material. On the one hand, Figs. 11(b) and 11(d) show a strong and clear return from the defect. Assuming the size of such defect is comparable to the wavelength (between 2 and 3 mm), its structure may resemble that of a corner reflector. Waves impinging the defect will be scattered back in approximately the same impinging direction, thus concentrating higher energy levels in that region.

On the other hand, Figs. 11(c) and 11(e), which depict measurements from the back side of the sample, show a different behavior. A lack of collected energy can be clearly observed due to the dispersive nature of a corner reflector imaged from the back side. The corner reflection assumption is schematically described in Figs. 12(a) and 12(b).

Other examples of aeronautics materials measured using the wide-beam approach are shown in Fig. 13. Sample GF_AH035 [Fig. 13(a)] containing a 0.35-ml water inclusion produces a lack of reflected energy in the SA image [Fig. 13(b)], since water is a remarkably weak scatterer

and dispersion is produced in all directions when assuming an oval-shaped inclusion [see Fig. 12(c)]. Due to the inherent way SA signals are measured and a lower spatial resolution, the low-reflectivity region appears larger than expected. Nevertheless, visual inspection can benefit from this smearing effect.

Rohacell-cored A-sandwiches containing debonds [Fig. 13(c)] produce prominent detections for the two sensors [Figs. 13(d) and 13(e)], but only traces are observed for the smallest defects. Although these small defects are slightly larger than the spatial resolution mentioned in Table 1, the low energy collected hinders clearer detections.

5 Conclusions

The possibilities of two measurement techniques based on a THz-FMCW imager have been studied: a focused and a wide-beam (SA) system. Although focused imagery presents good spatial resolutions but limited in-range imaging capabilities, SA imagery is a valid and simpler alternative for thicker samples, impacts, or water inclusions.

Based on the same test samples, the here underlying THz-FMCW measurements have been compared to THz time-domain spectroscopy and well-established NDT methods

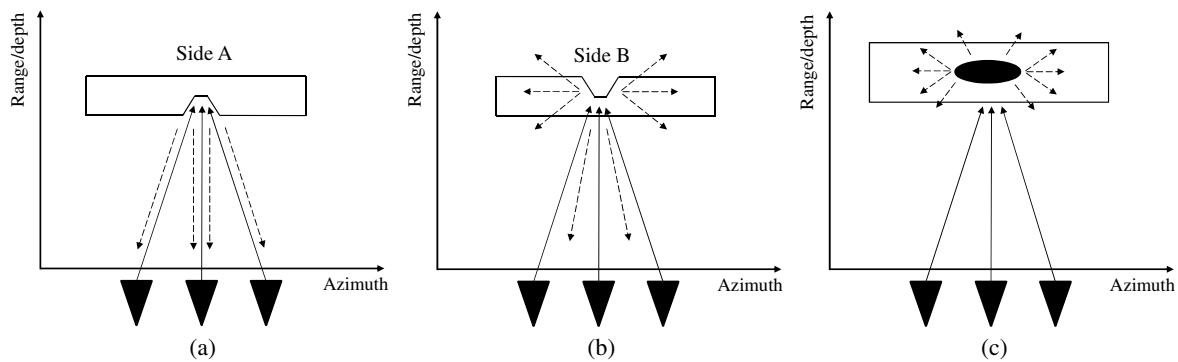


Fig. 12 Schematic representations of the effects observed when using wide-beam NDT on presented samples. (a) An impact is measured from side A, creating a corner reflector-like effect. (b) Most of the energy is scattered (dashed) in all directions when side B of the impacted sample is illuminated, obtaining very low energy levels. (c) Water inclusions produce very low scattering and almost isotropic dispersion.

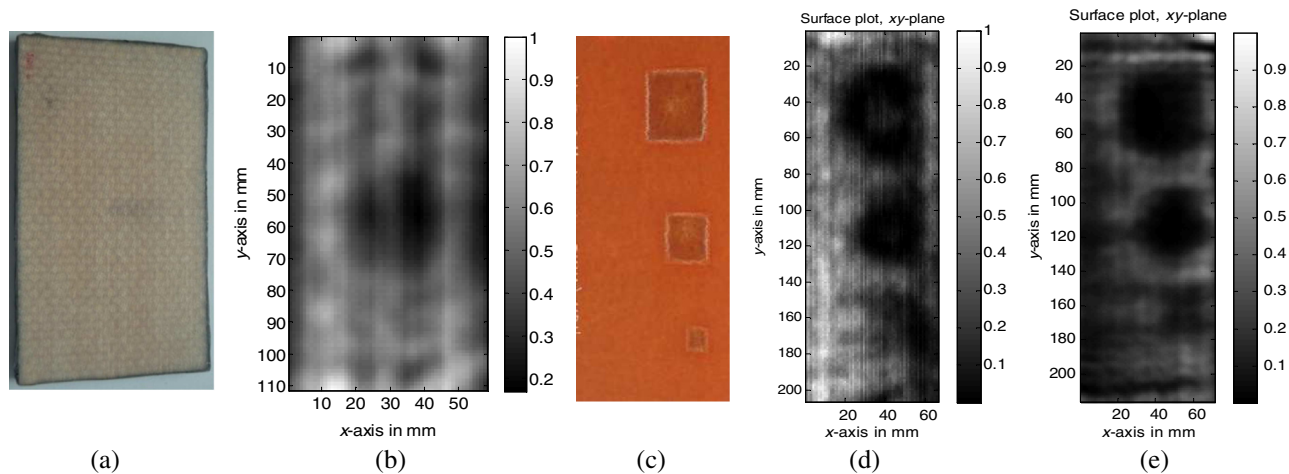


Fig. 13 Sample GF_AH035: (a) photograph of the sample. (b) Surface SA image at 100 GHz showing the water inclusion. Sample GF_AR: (c) photograph of the sample; (d) surface SA image at 100 GHz and (e), at 150 GHz.

such as infrared thermography, x-rays radiography, or ultrasound.^{22,23}

A case of special interest in which the THz-FMCW system can show its strengths are the proposed GFRP sandwich structures, since it is the only considered technique providing the capability to determine the inserts of the inspected test panels not only from the front side but also from the back side and therefore through their Rohacell or honeycomb cores. In case of inspecting thicker samples, in which front side and back side inspection may not be complete, the SA approach would be the only THz alternative.

Water inclusions and delaminations within these composites can best be inspected by optical infrared thermography, whereas x-ray radiometry is the only technique to retrieve foreign defects. Depending on the layer structure of the sandwich composite, ultrasonic measurements also deliver reasonable results, but cannot improve on the THz-FMCW inspections. However, due to the high absorption presented by water in the sub-THz frequency band, water inclusions were correctly located using SA measurements, although no clear shape was reported due to the limited spatial resolution.

The opposite is the case with GF reinforced solid laminates. Although the proposed THz-FMCW systems perform satisfactorily, except for delaminations and foreign defects, none of the considered techniques can compete with ultrasonic measurements, which allow the identification of all proposed defects with a very high success rate. Optical infrared thermography remains a good contactless alternative, as it is the only technique capable to reveal delaminations and shows the best results for impact damage detection.

Due to their electrical conductivity, CFRP composites cannot be penetrated by THz radiation and thus inner defects within these structures cannot be inspected. Nevertheless, depending on the size and type of surface defects, reflection measurements excluding wide-beam configurations can be used for surface inspection of these materials. Especially, THz time-domain spectroscopy is the technology of choice to identify coating misprocesses, whereas the optical infrared thermography and ultrasonic techniques are advantageous for impact damage inspection. In contrast, THz-FMCW measurements have shown that the present system is currently not feasible for the inspection of the proposed carbon fiber samples given the limited spatial resolution. Regarding surface inspections, where THz penetration depth is of minor importance, higher frequencies could be used to achieve a better spatial resolution. Furthermore, phase information of the measured signal can be used to potentially resolve surface deformations and varying thicknesses of transparent coating layers, whose depth variations are on the order of a tenth of the wavelength.²⁴ It has been shown that the THz techniques used could be complementary methods or even powerful alternatives. Furthermore, recent developments of sophisticated THz-FMCW systems have proven this technique to be capable for image acquisition at video rates.²⁵

Acknowledgments

The authors would like to thank Centro de Tecnologías Aeronáuticas (CTA, ES) and Appplus+ LGAI Technological Centre S.A. (ES) for their valuable contribution to this paper. This work was supported by the EU, FP7

DOTNAC project under Grant Agreement No. 266320, and the FhG Internal Programs under Grant No. Attract 018-692 158.

References

1. M. Tonouchi, "Cutting-edge terahertz technology," *Nat. Photonics* **1**, 97–105 (2007).
2. A. Redo-Sanchez et al., "Damage and defect inspection with terahertz waves," presented at *The Fourth International Workshop on Ultrasonic and Advanced Methods for Nondestructive Testing and Material Characterization*, North Dartmouth, MA (2006).
3. F. Rutz et al., "Terahertz quality control of polymeric products," *Int. J. Infrared Millimeter Waves* **27**(4), 547–556 (2006).
4. N. Karpowicz et al., "Compact continuous-wave subterahertz system for inspection applications," *Appl. Phys. Lett.* **86**(5), 054105 (2005).
5. S. Wietzke et al., "Terahertz imaging: a new non-destructive technique for the quality control of plastic weld joints," *J. Eur. Opt. Soc.* **2**, 07013 (2007).
6. C. Stoik, M. Bohn, and J. Blackshire, "Nondestructive evaluation of aircraft composites using transmissive terahertz time domain spectroscopy," *Opt. Express* **16**(21), 17039–17051 (2008).
7. N. Palka and D. Miedzinska, "Detailed non-destructive evaluation of UHMWPE composites in the terahertz range," *Opt. Quantum Electron.* **46**(4), 515–525 (2013).
8. E. Cristofani et al., "Assessment of 3D signal and image processing using FMCW THz signals," in *5th Int. Symposium on Optonics in Defense and Security, OPTRO 2012*, Paris, France (2012).
9. E. Cristofani and M. Vandewal, "High-resolution 3D SAR imaging applied to non-destructive testing of multi-layered materials," in *Proc. of the 9th European Conf. on Synthetic Aperture Radar (EUSAR)*, Nuremberg, Germany (2012).
10. E. Cristofani et al., "In-depth high-resolution SAR imaging using Omega-k applied to FMCW systems," in *2012 IEEE Radar Conf. (RADAR)*, Atlanta, GA, pp. 0725–0730 (2012).
11. J. J. M. de Wit, A. Meta, and P. Hoogetboom, "Modified range-Doppler processing for FM-CW synthetic aperture radar," *IEEE Geosci. Remote Sens. Lett.* **3**(1), 83–87 (2006).
12. M. Nezzadal, J. Schur, and L. Schmidt, "Non-destructive testing of glass fibre reinforced plastics with a synthetic aperture radar in the lower THz region," in *2012 37th Int. Conf. on Infrared, Millimeter, and Terahertz Waves (IRMMW-THz)*, Wollongong, NSW, pp. 1–2 (2012).
13. T. Chady and P. Lopato, "Testing of glass-fiber reinforced composite materials using terahertz technique," *Int. J. Appl. Electromagn. Mech.* **33**(3–4), 1599–1605 (2010).
14. P. Lopato, T. Chady, and R. Sikora, "Testing of composite materials using advanced NDT methods," *Int. J. Comput. Math. Electr. Electron. Eng.* **30**(4), 1260–1270 (2011).
15. R. Bogue, "New NDT techniques for new materials and applications," *Assembly Autom.* **32**(3), 211–215 (2012).
16. I. Amenabar, F. Lopez, and A. Mendikute, "In introductory review to THz non-destructive testing of composite mater," *J. Infrared Millimeter Terahertz Waves* **34**(2), 152–169 (2013).
17. Y.-K. Zhu et al., "A review of optical NDT technologies," *Sensors* **11**(8), 7773–7798 (2011).
18. H. Quast and T. Löffler, "3D-terahertz-tomography for material inspection and security," in *34th Int. Conf. on Infrared, Millimeter, and Terahertz Waves, 2009 (IRMMW-THz 2009)*, pp. 1–2 (2009).
19. M. Skolnik, *Introduction to Radar Systems*, McGraw-Hill, New York (1962).
20. H. Quast and L. Löffler, "3D-terahertz-tomography for material inspection and security," in *34th Int. Conf. on Infrared, Millimeter, and Terahertz Waves, 2009 (IRMMW-THz 2009)*, pp. 1–2 (2009).
21. I. G. Cumming and H. Wong, *Digital Signal Processing of Synthetic Aperture Radar Data: Algorithms and Implementation*, Artech House, Boston (2005).
22. "Assessment of NDT-THz potential in aeronautics," Technical Report: The DOTNAC Project Publications: Public Deliverable, http://www.sic.rma.ac.be/~ecristof/DOTNAC/TechRep_D734.pdf (2013).
23. M. Vandewal et al., "Advanced inspection of aircraft materials with THz sensors," in *8th Int. Conf. "Supply on the Wings"*, AIRTEC, Frankfurt/Main, Germany (2013).
24. B. Hils et al., "Terahertz profilometry at 600 GHz with 0.5 μm depth resolution," *Opt. Express* **16**, 11289–11293 (2008).
25. F. Friederich et al., "THz active imaging systems with real-time capabilities," *IEEE Trans. Terahertz Sci. Technol.* **1**(1), 183–200 (2011).

Edison Cristofani obtained his BEng and MEng degrees in telecommunications and electronics from the Autonomous University of Barcelona (ETSE-UAB, 2006) and the Technical University of Catalonia (ETSETB-UPC, 2008), respectively; majoring in radar/SAR systems, signal and image processing. Until 2010, he was a

research fellow at ETSETB-UPC, TSC Department. Since then he has been a research engineer for the Royal Military Academy of Belgium, CISS Department, working on SAR and compressive sensing. He is a PhD student.

Fabian Friederich studied optoelectronics at the University of Aalen, Germany, and received the PhD degree in physics from the Goethe University, Frankfurt am Main in 2012. In 2011, he joined the Institute of Technical Physics of the German Aerospace Center in Stuttgart. In 2013, he was granted a Fraunhofer Attract Award of the Fraunhofer Association to form a new research group at the Fraunhofer Institute for Physical Measurement Techniques IPM, Kaiserslautern, Germany.

Sabine Wohnsiedler received the diploma degree in meteorology from Universität Karlsruhe (TH)—Research University, now known as Karlsruhe Institute of Technology KIT, Germany, in 2006. She is a member of the Industrial Terahertz Measurement Techniques group at Fraunhofer Institute for Physical Measurement Techniques IPM, concentrating on material characterization and testing as well as on industrial implementation of terahertz technique.

Joachim Jonuscheit is a business development manager and is a deputy head of the department in the Materials Characterization and Testing (MC) department of the Fraunhofer Institute for Physical

Measurement Techniques IPM. He graduated in physics at the Ludwig-Maximilians University of Munich and received his PhD degree from the University of Erlangen-Nuremberg. He worked at various laser companies for several years in several management positions (project manager, R&D manager, and production manager).

Marijke Vandewal graduated in 1996 from the Royal Military Academy, Division Polytechnics, specialty telecommunications. In 2000, she became an assistant at the Royal Military Academy, in optronics, radar, and microwave techniques. In co-operation with Deutsches Zentrum für Luft- und Raumfahrt, she obtained in 2006 her PhD degree in engineering sciences. Since 2008, she has been teaching as a military professor at the Department of Communication, Information, Systems and Sensors of the Royal Military Academy.

René Beigang is a professor of experimental physics and head of the ultrafast photonics and THz physics group at the University of Kaiserslautern. He started his scientific career in the field of laser physics, nonlinear optics, atomic physics, and generation and application of ultrashort laser pulses. He has been working in the field of THz spectroscopy and applications for more than a decade.

Carsten Matheis: Biography is not available.